Supplementary Information

Towards Electrical Insulation Electromagnetic Interference Shielding Materials: Magnetic Network-Microcapacitors Framework for Advanced Electronics Packaging

Zeyu Zheng[a, b], Xinyin Gu[b], Yang Liu[b], Ting Xin[b], Jianhui Zeng[b], Jialin Wen[a], Hebin Zhang[b], Weijing Wu[a], Yan-Jun Wan[b *], Pengli Zhu[b, *], Rong Sun[b *]

[a] *State Key Laboratory of Luminescent Materials and Devices, South China University of Technology, Guangzhou 510640, People's Republic of China*

[b] *Shenzhen Institute of Advanced Electronic Materials, Shenzhen Institute of Advanced Technology, Chinese Academy of Sciences, Shenzhen 518055, China*

** Corresponding authors*

E-mail addresses: yj.wan@siat.ac.cn (Yan-Jun Wan), rong.sun@siat.ac.cn (Rong Sun), pl.zhu@siat.ac.cn (Pengli Zhu)

1. Supplementary Methods and Calculations

1.1 Liquid Phase Method Modified Reaction

During the solution-based modification process, a pH=5 is maintained, creating an acidic environment with a high concentration of H^+ ions in the solution. The surface Fe and Al in the powder react with H^+ and NO_3^- ions in the solution, undergoing the following reactions:

$$Al+3NO_3^-+6H^+=Al^{3+}+3NO_2+3H_2O$$

$$Fe+3NO_3^-+6H^+=Fe^{3+}+3NO_2+3H_2O$$

The generated Al^{3+} and Fe^{3+} ions combine with NO_3^- and acetate ions in the solution to form nitrates and acetates, which are subsequently adsorbed onto the surface of the FeSiAl particles. During the subsequent high-temperature calcination, the surface metal salts (such as $Al(NO_3)_3$, $(CH_3COO)_3Al$, $Fe(NO_3)_3$, and $(CH_3COO)_3Fe$, *etc*.) undergo decomposition reactions, forming Al_2O_3 and Fe_2O_3 (including Fe^{2+} oxide). Notably, due to the higher reactivity of Al^{3+} compared to Fe^{3+}, the resulting coating layer is predominantly composed of Al_2O_3.

1.2 Supplementary Materials and Methods:

FSAP@SiO_2, $Fe_{50}Ni_{50}$@SiO_2, and $Fe_{36}Ni_{64}$@SiO_2 particles were prepared using previously reported methods.[1] $Fe_{50}Ni_{50}$ and $Fe_{36}Ni_{64}$ (wt%) magnetic particles were obtained from Sichuan Green Forest Tech. CO., Ltd., China. Tetraethyl orthosilicate ($C_8H_{20}O_4Si$, 98%) and ammonium hydroxide solution were purchased from Macklin Biochemical Technology Co., Ltd. The experimental details were as follows: (1) magnetic particles were dispersed in an anhydrous ethanol solution (2 ml), and the dispersion was subjected to ultrasonication; (2) ammonia water was added under ultrasonic oscillation and stirred. (3) tetraethyl silicate (2 ml) was added, and the mixture was stirred at 50 °C; (4) magnetic particles with a SiO_2 coating layer were washed with ethanol multiple times and placed in an oven at 80 °C.

1.3 Methods for Evaluating Out-plane Thermal Conductivity

The thermal conductivity (k, W/m·K) was calculated using the equation:

$$k=\alpha\cdot\rho\cdot C_p \#(1)$$

where α is the thermal diffusivity, measured by the laser flash method (NETZSCH, LFA467); ρ is the density, calculated and measured by the Buoyancy Method; and C_p is the specific heat capacity of composites, measured by the Sapphire Method (TA, DSC2500).

1.4 Methods for Evaluating Electromagnetic Interference Shielding Efficiency

In this work, the formulas for the relevant electromagnetic shielding parameters are as follows:

$$R = |s_{11}|^2 \#(2)$$

$$T = |s_{21}|^2 \#(3)$$

$$A + T + R = 1 \#(4)$$

$$SE_R(dB) = -10\log(1 - R) \#(5)$$

$$SE_A(dB) = -10\log\left(\frac{T}{(1 - R)}\right) \#(6)$$

$$SE_{total}(dB) = SE_R + SE_A + SE_M \#(7)$$

where R, T, and A correspond to the power coefficients of the reflection, transmission and absorption, respectively. Moreover, the complex permeability μ_r and the complex permittivity ε_r were calculated by the following equations:

$$\mu_r = \mu_r^{'} - j\mu_r^{''} \#(8)$$

$$\varepsilon_r = \varepsilon_r^{'} - j\varepsilon_r^{''} \#(9)$$

which $\mu_r^{'}$, $\varepsilon_r^{'}$ and $\mu_r^{''}$, $\varepsilon_r^{''}$correspond to the real and imaginary parts of μ_r and ε_r, respectively. From this, $tan\delta_\mu$ and $tan\delta_\varepsilon$ could be calculated by the following equations:

$$tan\delta_\mu = \frac{\mu_r^{''}}{\mu_r^{'}} \#(10)$$

$$tan\delta_\varepsilon = \frac{\varepsilon_r^{''}}{\varepsilon_r^{'}} \#(11)$$

Besides, impedance matching Z_{in}/Z_0 was calculated by the following formula:

$$\frac{Z_{in}}{Z_0} = \sqrt{\frac{\mu_r}{\varepsilon_r}}\tanh\left[j\frac{2\pi}{c}\sqrt{\mu_r\varepsilon_r}fd\right] \#(12)$$

Here, Z_0 is the free space impedance (~377 Ω), Z_{in} represents the input impedance, and *d*, *f*, *c* means the thickness of sample, frequency, the velocity of light, respectively.

1.5 Methods for Calculating Coefficient of Thermal Expansion

The coefficient of thermal expansion (CTE) value for examples is calculated from the slope of the

TMA curves. The CTE value below (CTE1) and above (CTE2) glass transition temperature for examples is calculated from the slope of the TMA curves. CTE α for epoxy resin and its composites were calculated based on the thermal expansion curves using the provided,

$$\alpha = \frac{1}{L_0} \cdot \frac{\Delta L}{\Delta T} \# (13)$$

where L_0 is the initial length of epoxy resin and its composites, ΔL is the length change at an increased temperature (ΔT).

2 Supplementary Figures

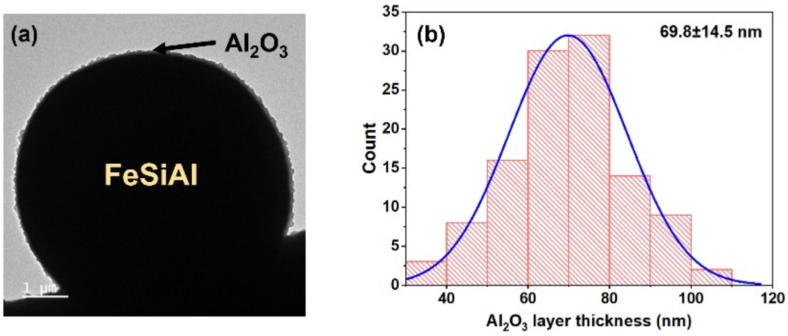

Figure S1. (a) High-resolution TEM image of the as-prepared typical FSAP@Al_2O_3 core-shell particle, and **(b)** the corresponding Al_2O_3 coating layer thickness distribution (69.8±14.5 nm).

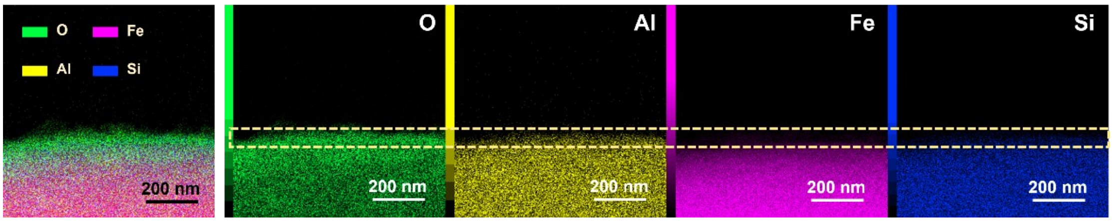

Figure S2. The element distribution (O, Al, Fe, Si elements) spectrum images of the alumina coating layer under transmission electron microscope.

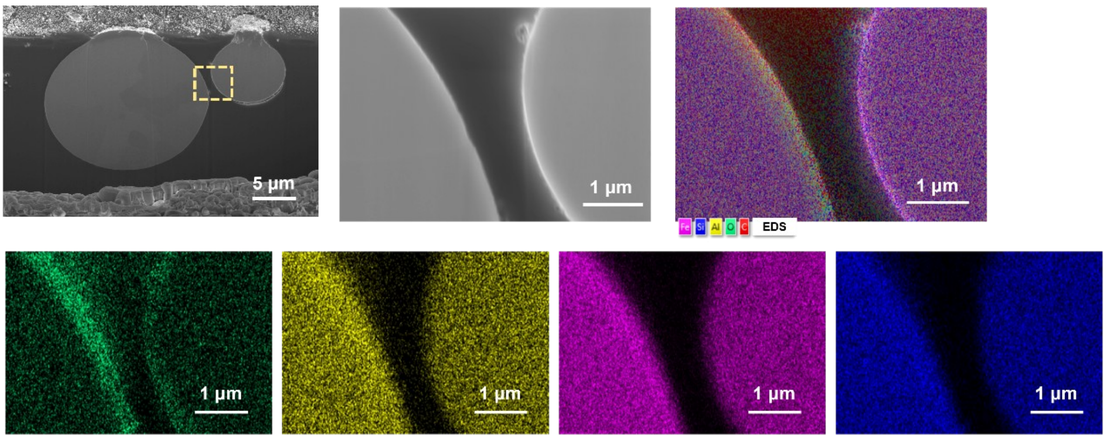

Figure S3. SEM and EDS images of FSAP@Al_2O_3 obtained by focus ion beam processing.

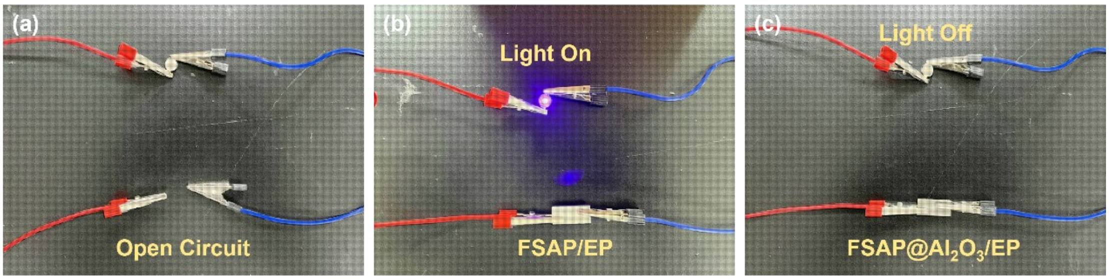

Figure S4. (a) The LED lighting test under **(b)** FSAP/EP and **(c)** FSAP@Al_2O_3/EP samples series connections.

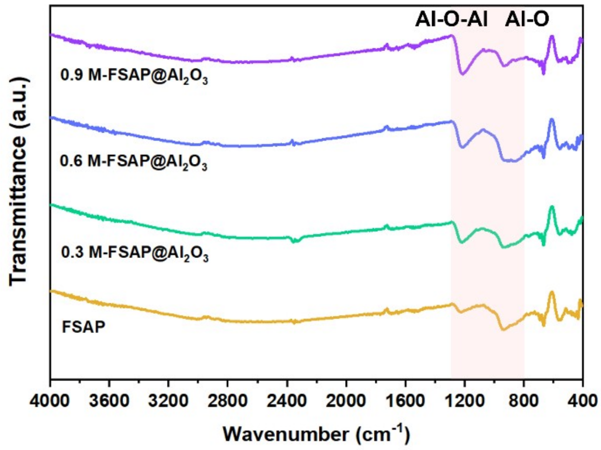

Figure S5. IR spectra images of the raw FSAP, and Al_2O_3-decorated FSAP with different precursor solution concentrations.

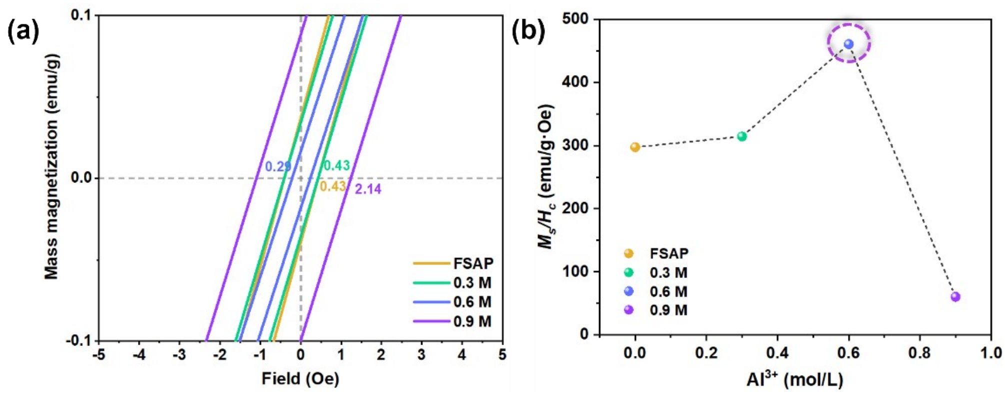

Figure S6. With the increase in the precursor solution Al^{3+} concentration, the hysteresis loop of FSAP and its composites show changes in **(a)** coercivity (H_c) and **(b)** the corresponding ratio to the saturation magnetization (M_s/H_c).

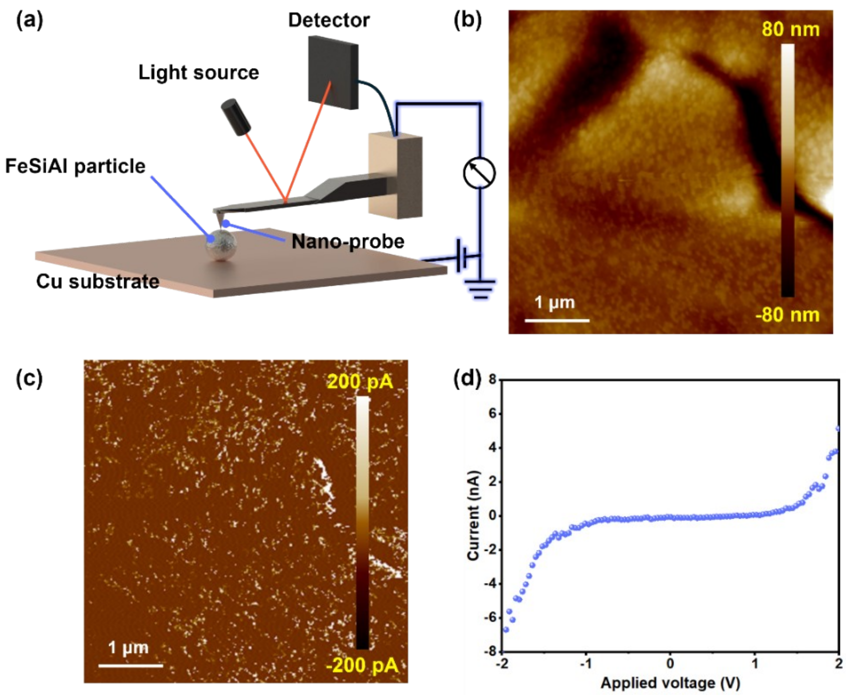

Figure S7. (a) Schematic diagram of conducting atomic force microscopy (CAFM) test. **(b)** Topography AFM image of FSAP and **(c)** the corresponding CAFM current mapping under an applied bias of 2 V. **(d)** I-V curve of FSAP surface (applied from -2 V to 2V).

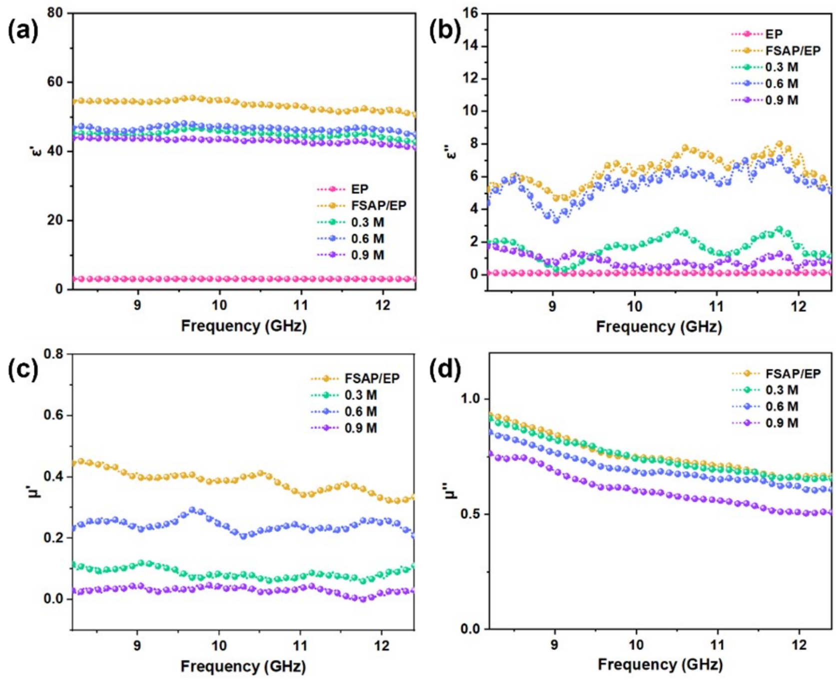

Figure S8. (a-d) Electromagnetic parameters FSAP and FSAP@Al_2O_3/EP under different precursor solution conditions.

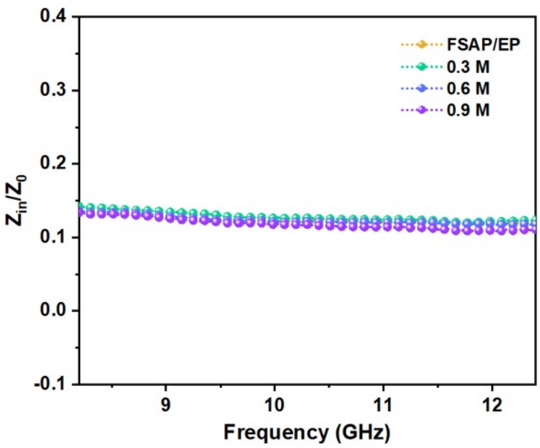

Figure S9. Impedance matching curves of different types of composites under gradient concentrations.

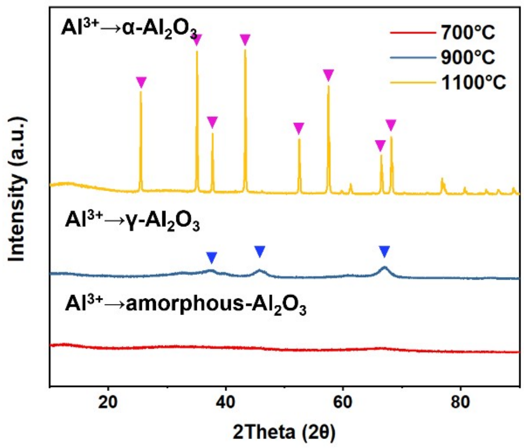

Figure S10. XRD spectra of the products obtained from the precursor solution at different calcination temperatures, without the addition of FSAP.

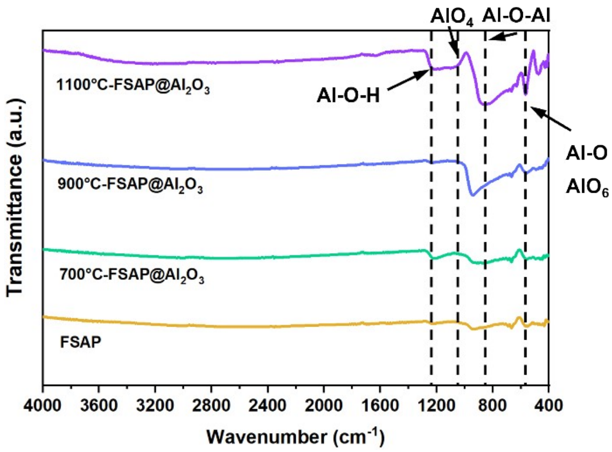

Figure S11. IR spectra images of the raw FSAP, and Al_2O_3-decorated FSAP with calcination temperatures.

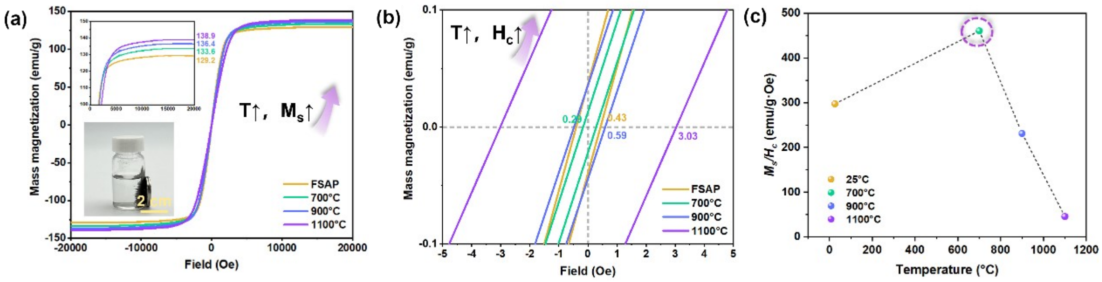

Figure S12. (a) Hysteresis loops of FSAP and different type of FSAP@Al_2O_3 particles. The inset shows saturation magnetization values. With the increase in calcination temperature, the hysteresis loop of FSAP and its composites show changes in **(b)** coercivity (H_c) and **(c)** the corresponding ratio to the saturation magnetization (M_s/H_c).

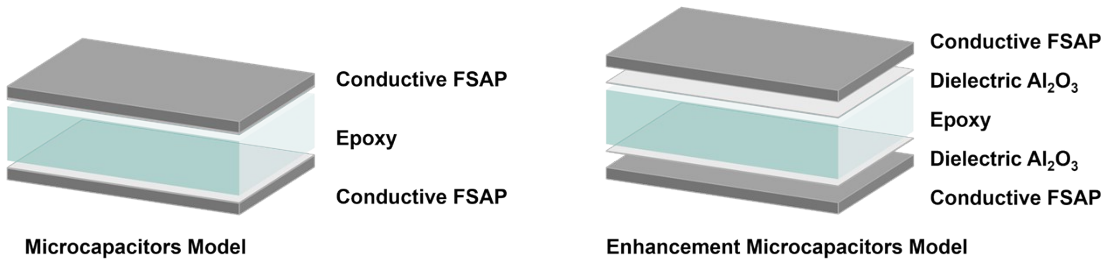

Figure S13. In this study, the microcapacitors structure model comprises FSAP as the conductive layer, epoxy, and Al_2O_3 as the dielectric layer. Microcapacitors model: FSAP/EP; Enhancement Microcapacitors model: FSAP@Al_2O_3/EP.

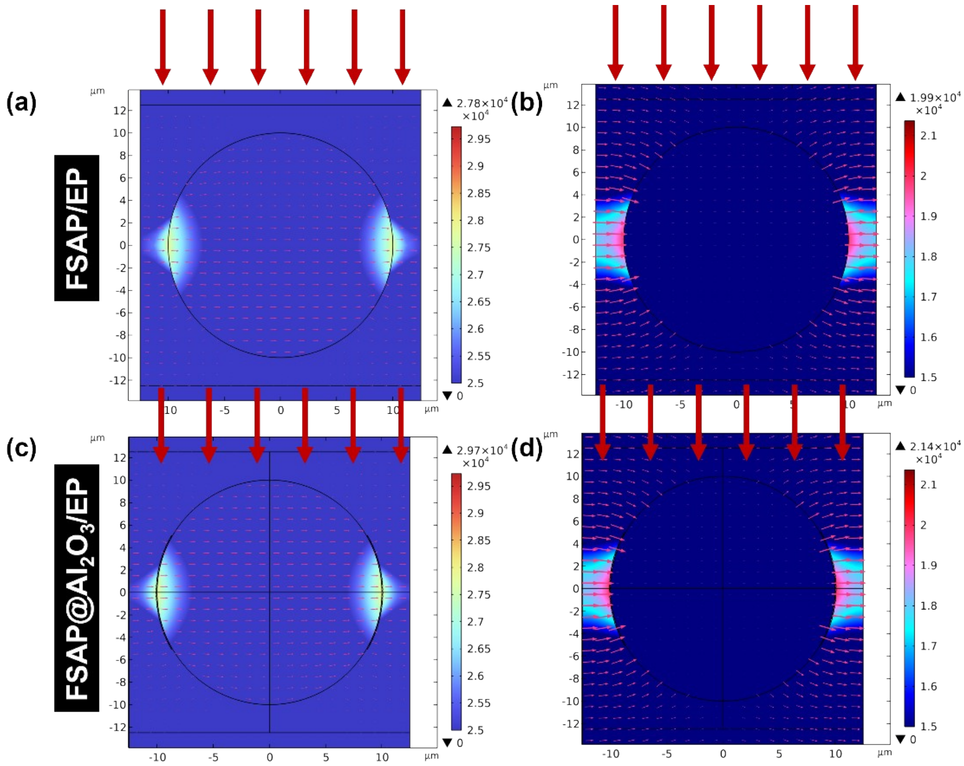

Figure S14. Simulation diagrams illustrating the **(a, c)** induced current density direction and **(b, d)** the response electric field direction under external electromagnetic wave input. The red arrows indicate the direction of electromagnetic wave incidence.

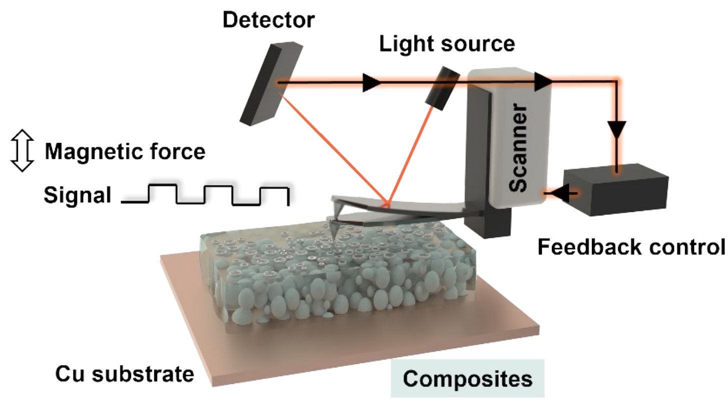

Figure S15. Schematic diagram illustrating the principle of magnetic force microscopy (MFM) for measuring the cross-section of polished composites.

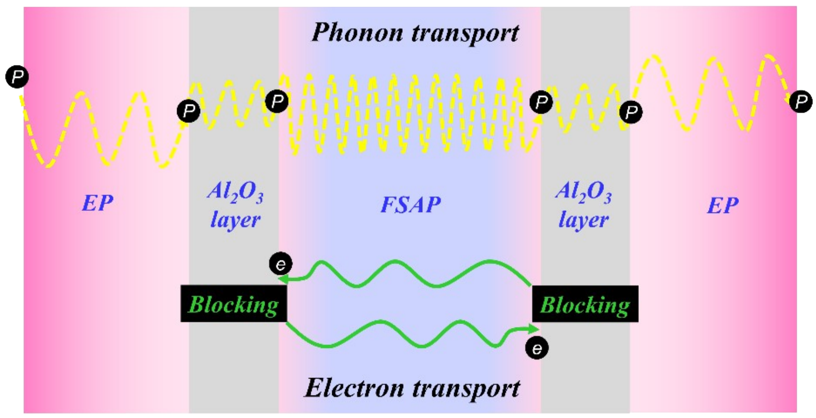

Figure S16. A schematic diagram illustrating the phonon and electron transport in constructed FSAP@Al_2O_3/EP composite.

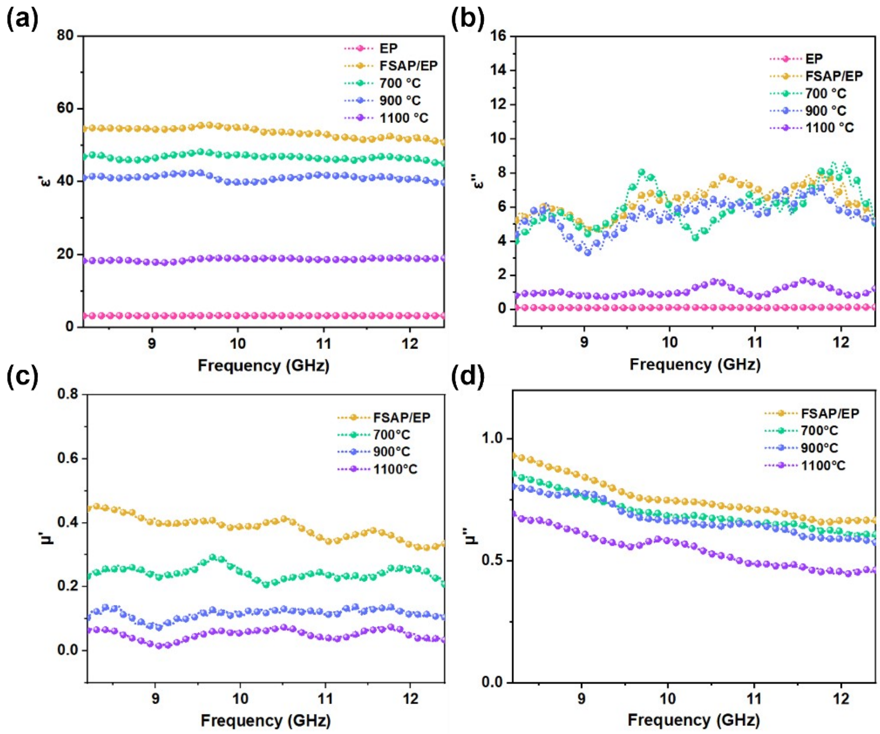

Figure S17. (a-d) Electromagnetic parameters FSAP and FSAP@Al_2O_3/EP under different calcination temperatures.

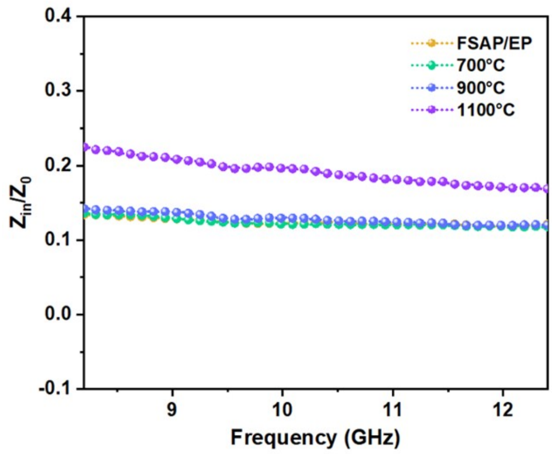

Figure S18. Impedance matching curves of different types of composites under gradient calcination temperatures.

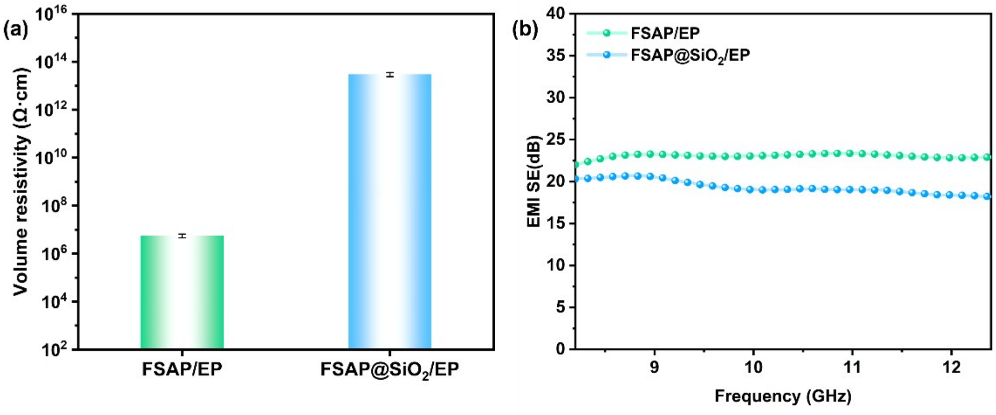

Figure S19. (a) Volume resistivity, **(b)** EMI shielding performance of FSAP/EP and FSAP@SiO_2/EP composites at 2 mm thickness.

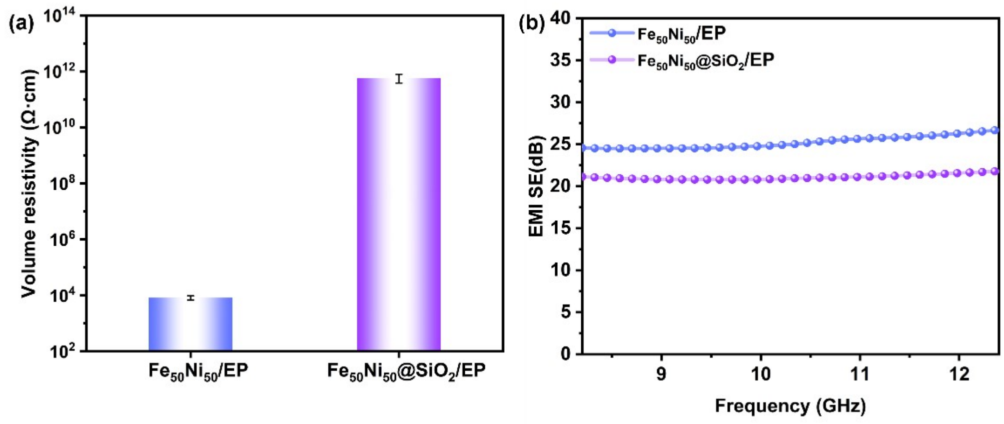

Figure S20. (a) Volume resistivity, **(b)** EMI shielding performance of $Fe_{50}Ni_{50}$/EP and $Fe_{50}Ni_{50}$@SiO_2/EP composites at 2 mm thickness.

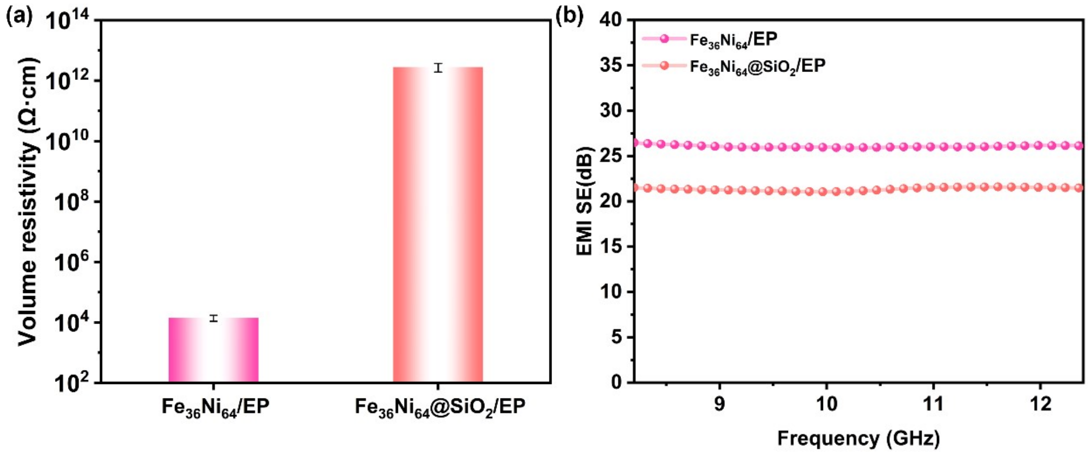

Figure S21. (a) Volume resistivity, **(b)** EMI shielding performance of $Fe_{36}Ni_{64}$/EP and $Fe_{36}Ni_{64}@SiO_2$/EP composites at 2 mm thickness.

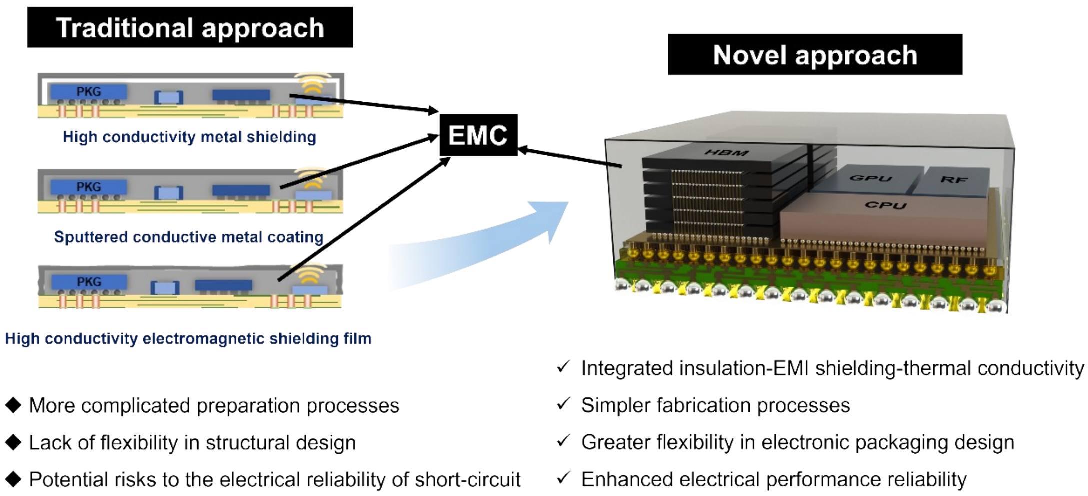

Figure S22. Advantages of the novel integrated "insulation-EMI shielding-thermal conductivity" epoxy composite materials in advanced electronic packaging.

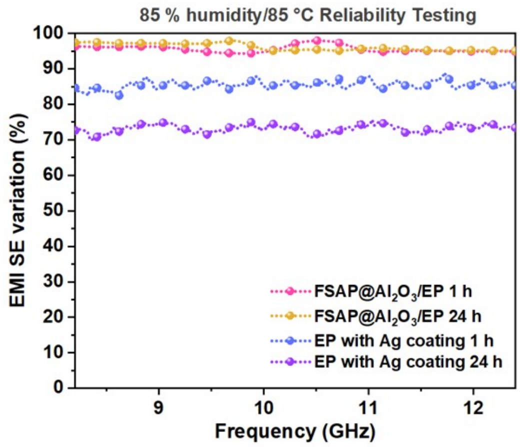

Figure S23. The variation curves of EMI SE for the prepared FSAP@Al_2O_3/EP composites and silver paste-coated epoxy resin under accelerated aging conditions of 85%/humidity/85 °C for 1 hour and 24 hours.

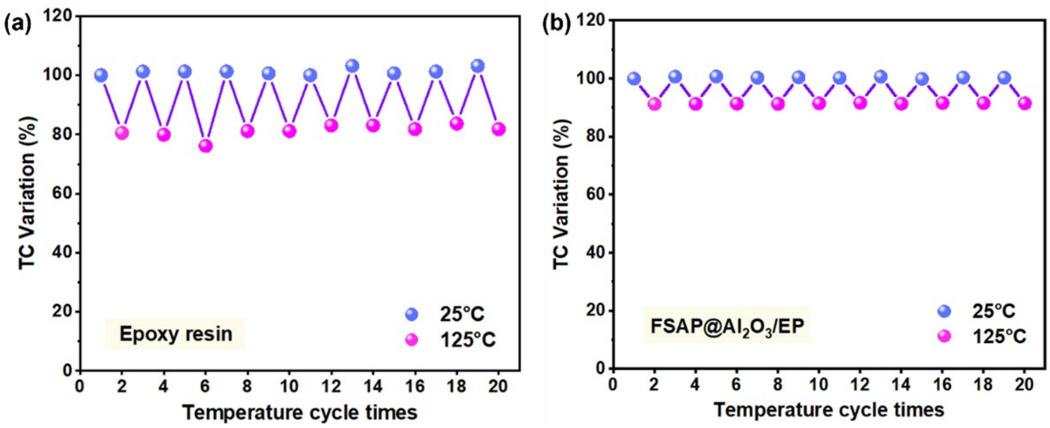

Figure S24. The TC variation curves of the **(a)** epoxy resin and the **(b)** prepared FSAP@Al_2O_3/EP composites under temperature cycling tests 25 °C-125 °C-25 °C.

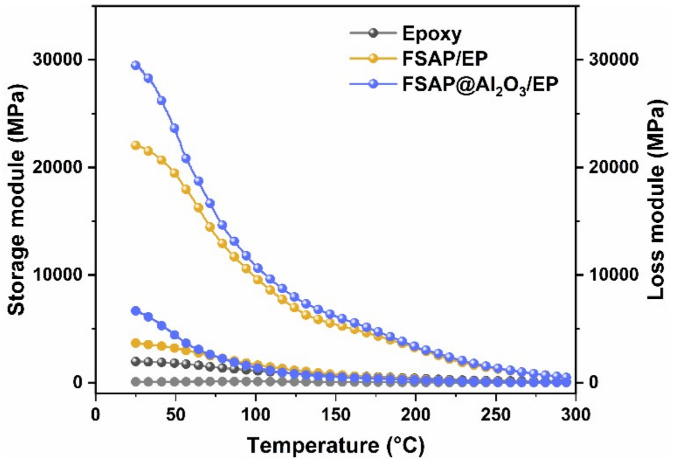

Figure S25. Storage and loss modulus curves of the insulation-electromagnetic shielding epoxy composites.

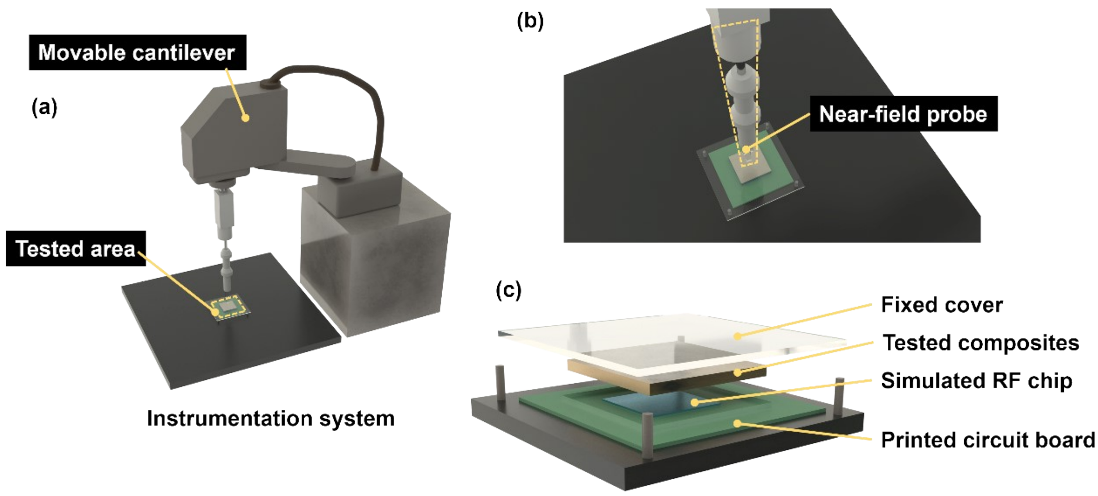

Figure S26. (a) Schematic diagram of the near-field EMI testing system during measurement, **(b)** magnified view of the tested area, and **(c)** illustration of the EMI shielding performance of the tested composites on a simulated Radio Frequency (RF) chip device.

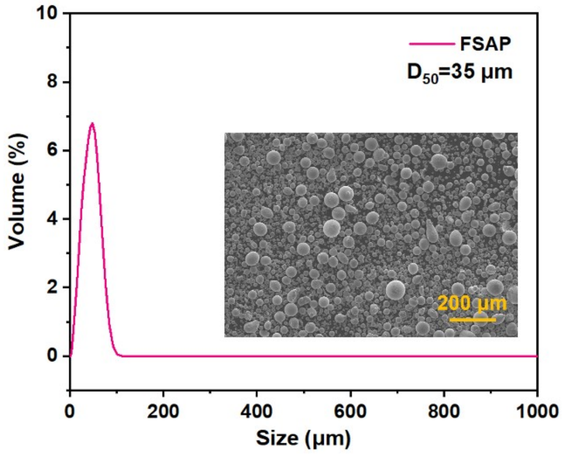

Figure S27. Size-volume distribution diagram of the original FeSiAl particles.

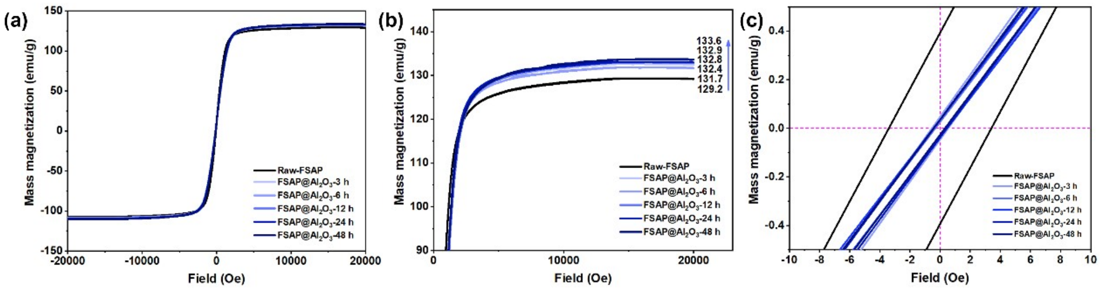

Figure S28. (a) Hysteresis loops of the modified FSAP under different liquid-phase modification reaction times, along with a comparison of the corresponding **(b)** maximum saturation magnetization and **(c)** coercivity.

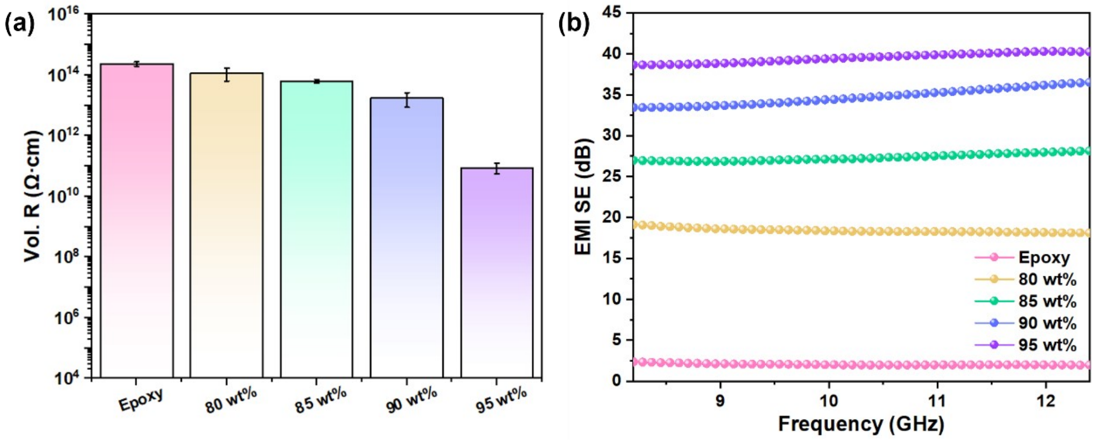

Figure S29. Evaluation of the **(a)** insulation properties and **(b)** EMI shielding ability of FSAP@Al_2O_3/EP (0.6 M) composites under gradient filler content.

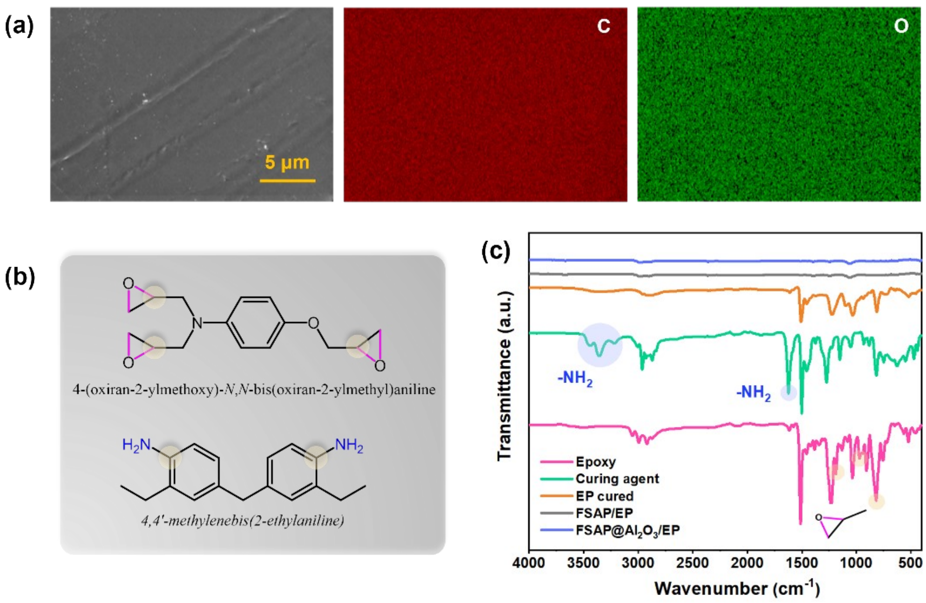

Figure S30. (a) SEM and EDS morphological images of epoxy after the curing reaction (180 °C, 2 h). **(b)** molecular formula information of epoxy resin and curing agent. **(c)** Infrared spectroscopy images of epoxy resin and its composites before and after curing.

3. Supplementary Tables

Table S1. Preparation parameters and naming conventions of epoxy-based composites involved in the study. The study involved three variables: precursor solution concentration (1, 2, 3), calcining temperature (2, 4, 5), and mass fraction variables (2, 6-8).

<table>
<tr><th>Scheme</th><th>Name</th><th>Precursor solution concentration</th><th>Calcination temperature</th><th>Filler loading</th></tr>
<tr><td>1</td><td>FSAP@Al_2O_3/EP</td><td>0.3 M</td><td rowspan="3">700 °C</td><td rowspan="6">90 wt%</td></tr>
<tr><td>2</td><td>FSAP@Al_2O_3/EP</td><td>0.6 M</td></tr>
<tr><td>3</td><td>FSAP@Al_2O_3/EP</td><td>0.9 M</td></tr>
<tr><td>2</td><td>FSAP@Al_2O_3/EP</td><td rowspan="3">0.6 M</td><td>700 °C</td></tr>
<tr><td>4</td><td>FSAP@γ-Al_2O_3/EP</td><td>900 °C</td></tr>
<tr><td>5</td><td>FSAP@α-Al_2O_3/EP</td><td>1100 °C</td></tr>
<tr><td>6</td><td>FSAP@Al_2O_3/EP</td><td rowspan="4">0.6 M</td><td rowspan="4">700 °C</td><td>80 wt%</td></tr>
<tr><td>7</td><td>FSAP@Al_2O_3/EP</td><td>85 wt%</td></tr>
<tr><td>2</td><td>FSAP@Al_2O_3/EP</td><td>90 wt%</td></tr>
<tr><td>8</td><td>FSAP@Al_2O_3/EP</td><td>95 wt%</td></tr>
</table>

Table S2. The electrical insulation properties, EMI shielding performance, and thermal conductivity of epoxy resin and its composites (“N/A” signifies “Not Applicable”).

<table>
<tr><th>Series</th><th>Filler loading</th><th>Vol. R (Ω·cm)</th><th>EMI SE (dB)</th><th>TC (W/m·K)</th></tr>
<tr><td>Epoxy</td><td>N/A</td><td>2.4E14</td><td>2</td><td>0.21</td></tr>
<tr><td>FSAP/EP</td><td rowspan="6">90 wt%</td><td>5.6E6</td><td>44</td><td>4.72</td></tr>
<tr><td>0.3 M-FSAP@Al_2O_3/EP</td><td>1.9E10</td><td>40</td><td>3.47</td></tr>
<tr><td>0.6 M-FSAP@Al_2O_3/EP</td><td>1.7E13</td><td>37</td><td>4.14</td></tr>
<tr><td>0.9 M-FSAP@Al_2O_3/EP</td><td>8.4E13</td><td>34</td><td>4.30</td></tr>
<tr><td>0.6 M-FSAP@γ-Al_2O_3/EP</td><td>2.9E14</td><td>28</td><td>3.38</td></tr>
<tr><td>0.6 M-FSAP@α-Al_2O_3/EP</td><td>2.5E15</td><td>19</td><td>4.71</td></tr>
</table>

Table S3. Comparison properties (volume resistivity, EMI SE, and out-plane thermal conductivity) of our electrically insulating FSAP@Al_2O_3/EP composite with other reported composites corresponding to **Figures 5d, e**.

Sample	**Volume resistivity /Ω·cm**	**EMI SE /dB**	**Out-plane TC (W/m·K)**	**Ref.**
PVA-PEG-SA	1.8×10^{5}	32.6	/	2
$TaSe_3$/EP	1.0×10^{7}	15.0	/	3
PPy/PEG/PVA	1.4×10^{7}	28.0	/	4
PS-S@SBS/Pyr	1.0×10^{8}	33.1	/	5
MXene/Al_2O_3/EP	1.2×10^{9}	22.3	2.10	6
GNP@PDMS/GF	3.5×10^{9}	50.1	1.47	7
PBAT@PLA/CNT	4.0×10^{9}	30.1	/	8
TPU/MWCNT/BN	1.0×10^{10}	53.6	0.93	9
LMPA/BNNS/EP	1.0×10^{11}	14.0	0.34	10
SiR/GNPs/BN	1.0×10^{12}	35.0	0.80	11
MXene/PDMS/BN	2.9×10^{12}	35.2	0.65	12
GNPs/BNNSs/CNF	4.1×10^{13}	29.0	/	13
MWCNT/SiC/HDPE	5.3×10^{13}	28.0	2.05	14
PP/AlN/MWCNT/BN	6.6×10^{13}	30.0	3.37	15
PVDF@MWCNT/BN	8.3×10^{14}	8.7	0.83	16
PMMA-CNT	1.3×10^{15}	11.0	2.05	17
FSAP@Al_2O_3/EP	**1.7×10^{13}**	**37.0**	**4.14**	**/**

Note: PVDF: polyvinylidene fluoride; MWCNT: Multiple walls carbon nanotube; BN: boron nitride; EP and ER: Epoxy resin; PP: Polypropylene; SiR: Silicon rubber; GNP: graphene nanoplatelets; PDMS: polydimethylsiloxane; TPU: Thermoplastic polyurethane; GF: graphene fluoride; SiC: silicon carbide; HDPE: High-density polyethylene; PMMA: Polymethyl methacrylate; CNT: Carbon nanotube; LMPA: low melting-point alloy; BNNS: boron nitride nanosheets; PPy: polypyrrole; PEG: polyethylene glycol; PVA: polyvinyl alcohol; SA: sodium alginate; SBS: styrene-butadiene-styrene; Pyr: pyrrhotite; PBTA: polybutylene adipate terephthalate; PLA: polylactic acid; CNF: cellulose nanofiber;

Table S4. Comparison of parameters of electrical insulation-EMI shielding epoxy composites with commercial epoxy molding compounds for electronic packaging.

Manufacturer information	**Filler content/type**	**TC (W/m·K)**	**CTE1/CTE2 (ppm/℃)**	**Volume resistivity (Ω·cm)**	**Modulus (GPa)**	**EMI SE**
KYOCERA	89 wt% Al_2O_3/SiO_2	3.0	12/46	＞5.0×10^{12}	/	/
KYOCERA	Al_2O_3/SiO_2	2.3	20/60	＞5.0×10^{12}	/	/
HITACHI	88.5 wt% Al_2O_3/SiO_2	3.0	12/48	/	22	/
DOiTECH	90 wt%-Al_2O_3	3.0	10/38	＞5.0×10^{13}	27	/
DOiTECH	91 wt%-Al_2O_3	5.0	10/35	＞5.0×10^{13}	33	/
This work	90 wt%-FSAP@Al_2O_3	4.14	19/75	＞1.0×10^{13}	29	**37 dB**

Reference

1. H. C. Wangchang Li, Yue Kang, Yao Ying, Jing Yu, Jingwu Zheng, Liang Qiao, Ye Jiang, Shenglei Che, *Acta Mater.*, 2019, **167**, 267-274.
2. Y. Xu, M. Pei, J. Du, R. Yang, Y. Pan, D. Zhang and S. Qin, *New J. Chem.*, 2023, **47**, 13721-13728.
3. Z. Barani, F. Kargar, Y. Ghafouri, S. Ghosh, K. Godziszewski, S. Baraghani, Y. Yashchyshyn, G. Cywiński, S. Rumyantsev, T. T. Salguero and A. A. Balandin, *Adv. Mater.*, 2021, **33**, 2007286.
4. S. Lu, B. Ouyang, S. Han, F. Qiao, K. Chen, F. Wu, A. Xie, E. Kan and H. Zeng, *ACS Appl. Mater. Inter.*, 2022, **5**, 11407-11413.
5. Z. Wang, J. Su, J. Wang, Y. Feng, Q. Xu, H. Wang and H. Jiang, *Chem. Eng. J.*, 2024, **498**, 155065.
6. F. Guo, Y. Wang, K. Xue, L. Liu, J. Li and Y. Huang, *Compos. Sci. Technol.*, 2024, **248**, 110425.
7. M. C. V. Sebastian Anand, Dineshkumar Mani, Jun-Beom Kim, Tae-Hyeong Jeong, Md. Akhtarul Islam, Sung-Ryong Kim, *Chem. Eng. J.*, 2023, **462**, 142017.
8. T. Liu, H. Feng, C. Jin, M. Pawlak, M. R. Saeb and T. Kuang, *Chem. Eng. J.*, 2024, **493**, 152438.
9. G. Wang, X. Liao, F. Zou, P. Song, W. Tang, J. Yang and G. Li, *Compos. Commun.*, 2021, **28**, 100953.
10. P. Zhang, R. Tian, X. Zhang, X. Ding, Y. Wang, C. Xiao, K. Zheng, X. Liu, L. Chen and X. Tian, *Compos. Part B-Eng.*, 2022, **232**, 109611.
11. C.-P. Feng, S.-S. Wan, W.-C. Wu, L. Bai, R.-Y. Bao, Z.-Y. Liu, M.-B. Yang, J. Chen and W. Yang, *Compos. Sci. Technol.*, 2018, **167**, 456-462.
12. H. Liu, R. Fu, X. Su, B. Wu, H. Wang, Y. Xu and X. Liu, *Compos. Commun.*, 2021, **23**, 100593.
13. J. Yun, J. Lee, J. Kim, J. Lee and W. Choi, *Carbon*, 2024, **228**, 119397.
14. X. Zhang, J. Zhang, L. Xia, J. Wang, C. Li, F. Xu, X. Zhang, H. Wu and S. Guo, *Chem. Eng. J.*, 2018, **334**, 247-256.
15. Y. Zhang, B. Tang, Y. Liu, R. Feng, S. Song, C. Xiong and L. Dong, *Polym. Composite*, 2020, **41**, 1673-1682.
16. P. Zhang, X. Ding, Y. Wang, Y. Gong, K. Zheng, L. Chen, X. Tian and X. Zhang, *Compos. Part A-Appl. S.*, 2019, **117**, 56-64.
17. K. Hayashida and Y. Matsuoka, *Carbon*, 2015, **85**, 363-371.